Environmental Science and Pollution Research (2021) 28:23568–23581
https://doi.org/10.1007/s11356-020-09178-1

ADVANCED OXIDATION/REDUCTION TECHNOLOGIES: AN PERSPECTIVE FROM IBEROAMERICAN COUNTRIES

Facile fabrication of hybrid titanium(IV) isopropoxide/pozzolan nanosheets (TnS-Pz) of high photocatalytic activity: characterization and application for Cr(VI) reduction in an aqueous solution

Aline M. Novack[1] · Glaydson S. dos Reis[2] · Fabíola V. Hackbarth[1] · Belisa A. Marinho[1] · Maja B. Đolić[3] · José A. B. Valle[1] · Carlos H. Sampaio[4] · Eder C. Lima[5] · Guilherme L. Dotto[6] · Antônio Augusto Ulson de Souza[1] · Vítor J. P. Vilar[7] · Selene M. A. Guelli Ulson de Souza[1]

Received: 11 February 2020 / Accepted: 4 May 2020 / Published online: 30 May 2020

Abstract

This paper presents the synthesis of a hybrid material through the use of natural pozzolan and titanium(IV) isopropoxide using the sol-gel method and its application in the photocatalytic hexavalent chromium reduction. The characterization data indicated a mesoporous material possessing a surface area of 271.7 $m^2\ g^{-1}$. The morphology studies (SEM and TEM) showed nanosheet hybrid structures. The analysis of DRUV, FTIR, XRD, and Mössbauer spectroscopy provides a different electronic structure of the synthetized material when compared with the originals, proving the hybridization process between pozzolan and titanium(IV) isopropoxide**.** The photocatalytic reduction of Cr(VI) to Cr(III) using the hybrid material showed a better performance than conventional photocatalysts (precursor and TiO_2-P25). Operational conditions such as chromium initial concentration (0.02–0.20 mM), solution pH (3–6), and type of scavenger (citric or tartaric acid) were evaluated in order to determine the best experimental conditions for the Cr(VI) photoreduction. At their optimum (catalyst load of 15 mg L^{-1}, tartaric acid as scavenger, $[\text{scavenger}]_0/[\text{Cr(VI)}]_0$ M ratio = 3:1, pH 3, and 25 °C), the total photoreduction of 0.20 mM Cr(VI) was achieved in 180 min. The novel hybrid materials synthesized from pozzolan and titanium(IV) isopropoxide showed to be a potential catalyst for the Cr(VI) reduction in aqueous solution.

Aline M. Novack and Glaydson S. dos Reis contributed equally to this work.

Highlights

- Facile fabrication of hybrid titanium(IV) isopropoxide/pozzolan nanosheets
- Ti–O–Si and Ti–O–Al bonds between the titanium(IV) isopropoxide and pozzolan
- Innovative hybrid pozzolan-based material for Cr(VI) photocatalytic reduction
- A novel photocatalyst with a short bandgap and high S_{BET}

Responsible editor: Ioannis A. Katsoyiannis

Electronic supplementary material The online version of this article (https://doi.org/10.1007/s11356-020-09178-1) contains supplementary material, which is available to authorized users.

✉ Belisa A. Marinho
belisamarinho@gmail.com

✉ Vítor J. P. Vilar
vilar@fe.up.pt

Extended author information available on the last page of the article

Keywords Titanium(IV) isopropoxide/pozzolan synthesis · Hybrid material · Heterogeneous photocatalysis · Metal photoreduction

Introduction

Several thorough studies have concluded that TiO_2-based materials are the most efficient photocatalysts to promote oxidation and reduction reactions, regarding the removal of a wide range of organic and inorganic compounds (Choi et al. 2001; Dong et al. 2015; Eskandarloo et al. 2015; Marinho et al. 2017b; Yang and Lee 2006). However, these materials usually exhibit unsatisfactory photocatalytic efficiency due to their restricted visible-light absorption capacity (Wang et al. 2018b), as well as low surface area and easy recombination of charge carriers (Guayaquil et al. 2017). Therefore, a number of modification approaches are adopted to enhance the materials' photocatalytic performance, such as manufacturing a nano/mesoporous structure (Adán et al. 2007; Avansi et al. 2014; Guayaquil et al. 2017; Pongwan et al. 2016), combining them with other semiconductors (El Mragui et al. 2019; Qin et al. 2019), and doping and hybridizing them with non-metal (Khedr et al. 2017; Patil et al. 2019) or metal atoms (Adán et al. 2007; Lei et al. 2014b; Pongwan et al. 2016). This element doping strategy plays an essential role in tuning the bandgap structure, extending their light absorption, increasing their charge transfer mobility, and creating more active surface sites (Yan et al. 2013).

Other photocatalysts have also been investigated, including materials based on copper (Huang et al. 2017b), zinc (Gholami et al. 2016), and iron (Roonasi and Mazinani 2017) oxides, as well as cadmium (Wang et al. 2017) and zinc (Wang et al. 2017) sulfides. Although these photocatalysts may present high efficiency in the photo-oxidation/photoreduction of several organic and inorganic pollutants, they also present high preparation costs, making the process expensive and infeasible from a practical point of view. Thus, photocatalytic enhancement using natural, abundant, and cheap raw materials has become attractive in the area of photocatalysis.

Pozzolan is a natural and abundant low-cost resource, consisting mainly of SiO_2, Al_2O_3, and Fe_2O_3 oxides (Wamba et al. 2017). Italy, Chile, Greece, and Cameroon (Wamba et al. 2017) have deposits of this material and process 3000, 915, 900, and 600 kt/year, respectively. Natural pozzolan is used as a raw material in cement factories and in water treatment as an adsorbent (Wamba et al. 2017). Although studies have focused on natural pozzolans used for improving the performance and durability of self-compacting concrete (Moon et al. 2014; Omrane et al. 2017), only a few studies have concentrated on these materials under enhanced visible-light photocatalysis (Lackhoff et al. 2003; Wang et al. 2018a).

Even though or despite the fact natural pozzolan exhibits poor photocatalytic performance, the mixing of a natural pozzolan with titanium(IV) isopropoxide was an attempt to create an innovative photocatalyst, through a facile and affordable way.

Unlike most organic pollutants, heavy metal ions are not biodegradable into harmless end products as CO_2 and H_2O (Carolin et al. 2017). Heavy metals are found in wastewater from many types of industries such as chemical, petrochemical, mining, and metallurgical (Carolin et al. 2017; Enuneku et al. 2017). Photocatalysis has been applied successfully over the last few years in treating a wide range of wastewaters polluted with inorganic compounds, including Cr(VI) (Byrne et al. 2017; Soares et al. 2016). Cr(VI) is known as potentially carcinogenic and mutagenic (Trejo-Valdez et al. 2019). The mechanism of the direct photocatalytic reduction of Cr(VI) occurs when semiconductors are excited by UV radiation, leading to the generation of an electron/hole pair (Kumar and Chowdhury 2018). These photogenerated electrons are transferred from the semiconductor conduction band to the chromium species; in parallel, the positive holes can react with H_2O/HO^- producing $HO^\bullet$ radicals (Litter 2015). Positive holes and $HO^\bullet$ radicals can result in the reoxidation of Cr(III) to Cr(VI) (Kumar and Chowdhury 2018). In addition, the electron-hole recombination can also suppress the reaction. Several organic agents (oxalic, citric, tartaric acid, etc.) are often added as sacrificial agents, reacting with the $HO^\bullet$ radicals or holes and hindering the electron-hole recombination, boosting the Cr(VI) reduction efficiency (Litter 2015). The organic acid oxidation can result in the formation of strong reducing agents ($HCOO^{\bullet-}$), able to promote an indirect Cr(VI) reduction in the solution bulk (Marinho et al. 2018; Meichtry et al. 2011).

The main goal of this work is the development of a novel hybrid material synthetized from pozzolan and titanium(IV) isopropoxide, as a potential catalyst for the Cr(VI) reduction in aqueous solution. The reduction rate was evaluated as a function of Cr(VI) initial concentration, solution pH, and type of scavenger used to avoid the reoxidation of Cr(III) to Cr(VI).

Materials and methods

Chemicals, reagents, and solutions

All solutions were prepared using deionized water. Chemicals of an analytical grade were used: ethanol (Merck, 99.99%), titanium(IV) isopropoxide (Aldrich, 97%), potassium dichromate (Aldrich, 99.9%), nitric acid (Aldrich, 65%), and sodium hydroxide (Aldrich, 98%). The Cr(VI) solution was prepared by dissolving potassium dichromate ($K_2Cr_2O_7$) in deionized water.

Synthesis of titanium(IV) isopropoxide nanosheets

Titanium(IV) isopropoxide nanosheets (TnS) were prepared by mixing a solution of ethanol (125 mL) and titanium(IV) isopropoxide (1.25 mmol of Ti(IV)). The suspension was agitated for 1 h. Then, 1.3 mL of water mixed in 50 mL of ethanol was added drop by drop in the suspension. In sequence, the mixture was agitated for 1 h again. The dispersion was centrifuged at 3500 ppm (5 min) and dried in an oven at 80 °C for 4 h. The obtained material was hydrothermally treated in a Teflon reactor with sodium hydroxide solution (10 M) at 140 °C for 36 h. The resultant material was neutralized with nitric acid (3 M) and washed with distilled water until a near-neutral pH (6.6) was obtained. The material was then dried at 100 °C for 24 h.

Natural pozzolan

Natural pozzolan (Pz) was collected on the Cameroon Volcanic Line in Adamawa, Cameroon. The coarse natural pozzolan collected was crushed, sieved, washed, and dried at 105 °C for 24 h in an oven. The dried pozzolan was then pulverized in an agate mortar. The obtained powder was sieved in order to achieve a fraction lower than 53 μm for further chemical modification.

Synthesis of hybrid titanium(IV) isopropoxide/pozzolan nanosheets

Hybrid/pozzolan nanosheets (TnS-Pz) were prepared by mixing natural pozzolan in a solution of ethanol (125 mL) and titanium(IV) isopropoxide (1.25 mmol of Ti(IV) per mass of material). The dispersion was agitated at room temperature for 1 h. Then, 1.3 mL of water mixed in 50 mL of ethanol was added drop by drop in the suspension. In sequence, the mixture was agitated for another 1 h. The dispersion was centrifuged at 3500 rpm (5 min) and dried in an oven at 80 °C for 4 h. The material obtained was hydrothermally treated in a Teflon reactor with a sodium hydroxide solution (10 M) at 140 °C for the 36 h. The resultant material was neutralized using nitric acid (3 M) and washed with distilled water until a near-neutral pH (6.6) was achieved.

The material obtained was then dried at 100 °C for 24 h and kept in plastic tubes for further characterization and applications. An overview of the preparation of the TnS-Pz (Fig. S1A) as well as the scheme of the chemical bond between the titanium and pozzolan (Fig. S1B) is presented in the supplementary material.

Nanosheet material characterization

Nitrogen adsorption isotherms were recorded with a commercial system at − 196 °C after drying for 3 h at 120 °C under low pressure (< 2 mbar). The surface area was determined using the Brunauer, Emmett, and Teller (BET) method. A scanning electron microscope (SEM) equipped with an energy-dispersive X-ray spectroscope (EDX) (TESCAN 3, Sweden) and transmission electronic microscope (TEM) (JEOL JEM-1200 Exll) were both used to observe the surface morphologies and elemental composition.

A Bruker spectrometer of the alpha model Fourier transform infrared spectroscopy (FTIR) with an ATR (attenuated total reflectance) accessory was used to determine the functional groups of the hybrid materials. Sixty-four cumulative scans over the 4000–400 cm^{-1} range at a resolution of 4 cm^{-1} recorded the spectrum.

A Shimadzu UV-2450 spectrophotometer, using an ISR-2200 Integrating Sphere Attachment at a spectral range of 200–900 nm, provided the ultraviolet-visible diffuse reflectance (DRUV) and diffuses reflectance. In this analysis, the samples were treated as powder. $BaSO_4$ (Wako Pure Chemical Industries, Ltd.) was used to obtain the baseline. All measurements were carried out at room temperature (25 °C ± 2).

The TnS-Pz samples were analyzed in X-ray diffraction instruments (BRUKER-Diffrac 5000 and PanAnylical-*Xpert* MPD) operating at 45 kV and 40 mA using Cu-Kα monochromatic radiation ($\lambda = 1.5418$ Å), 2θ angle interval from 2 to 100° with step sizes of 0.016° and counting time of 60 s by step, slit widths of 200 μm (D5000), and Xcelerator linear detector with active window of 2.122° (Xpert MPD).

The morphological structure was tested using the X-ray diffraction (XRD) method, performing an ENRAF NONIUS FR590 XRD (Bruker AXS, MA, USA) diffractometer at Cu K_α 1.2 radiation and a step/time scan mode of 0.05 s^{-1}. The XRD pattern of TnS-Pz sample was compared with the diffraction powder file (PDF2) for the following components: diopside aluminian (reference pattern 01-086-0004), anatase, syn (TiO_2) (01-089-4221), calcium aluminum silicat ($Ca(Al_2Si_2O_8)$) (01-087-1616), hematite, syn (Fe_2O_3) (01-089-8103), and titanomagnetite ($Fe_{2.5}Ti_{0.50}O_4$), syn (01-075-1377).

The ^{57}Fe-Mössbauer spectra (Wissel spectrometer) were collected at room temperature under standard transmission geometry in constant acceleration mode where a ^{57}Co source was embedded in the rhodium matrix. The spectrometer was calibrated according to the spectrum of natural iron. The Mössbauer spectra were fitted by the

WinNormos-DIST program (Brand 2008). The isomer shift values (δ) are quoted relative to natural iron ($\delta = 0$).

Photocatalysis experimental procedure

The Cr(VI) reduction reactions were performed in a lab-scale annular photoreactor (Fig. S2), as reported elsewhere (Marinho et al. 2017a; Salim et al. 2016). The Supplementary Material presents a detailed description of the photoreactor.

The recirculation glass vessel of the lab-scale prototype was filled with 1.5 L of Cr(VI) solution (0.02–0.20 mM), which was pumped into the annular photoreactor and homogenized by recirculation in the closed system for 15 min in complete darkroom conditions ($Q = 1.6$ L min^{-1}). The temperature set-point of the refrigerated thermostatic bath was adjusted to maintain the intended solution temperature (25 °C). After which, an organic acid scavenger, citric acid or tartaric acid, was added, tested at $[\text{scavenger}]_0/[\text{Cr(VI)}]_0$ M ratio of 3:1 (based on previous results as reported in the work of Vilar and co-workers (Marinho et al. 2016)), and the pH was adjusted from 3.0 to 6.0, using sulfuric acid/sodium hydroxide. After that, the photocatalyst was added at a concentration of 15 g L^{-1} and the UVA-Vis lamp was turned on. Samples were taken after each addition before turning on the UVA-Vis lamp (Philips Actinic BL TL 6W/10 1FM/10X25CC), and during the photoreduction period at predetermined times. Fig. S3 shows the spectral power distribution of the UVA-Vis lamp. Other assays were also performed under the following conditions in order to verify the influence of each component: (i) the absence of a catalyst; (ii) the absence of a scavenger; (iii) the absence of a catalyst and a scavenger; (iv) the absence of a scavenger and light.

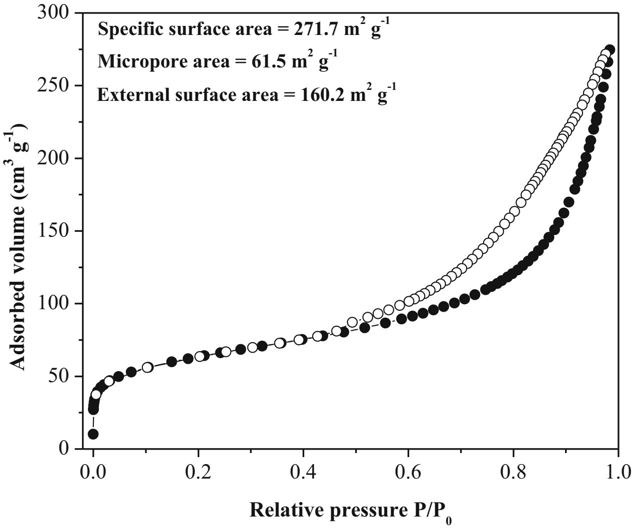

Fig. 1 N_2 adsorption-desorption isotherms of pure pozzolan and TnS-Pz. (●) adsorption, (○) desorption

Ferrioxalate actinometry (6 mM of Fe(III) and 30 mM of oxalic acid) determined a photonic flux reaching the reaction medium of 1.67×10^{-6} einstein s^{-1}, corresponding to a radiant power of 0.56 W ($\Phi = 1.25$ (Kuhn et al. 2004)). Total chromium concentration was determined by atomic absorption spectrometry (AAS, Shimadzu model AA 6300) using an air-acetylene flame. Cr(VI) concentration was evaluated by molecular absorption spectrophotometry. The procedure followed was based on the formation of a pink complex of Cr(VI) with 1.5-diphenylcarbazide in acid solution, with maximum absorbance at 540 nm.

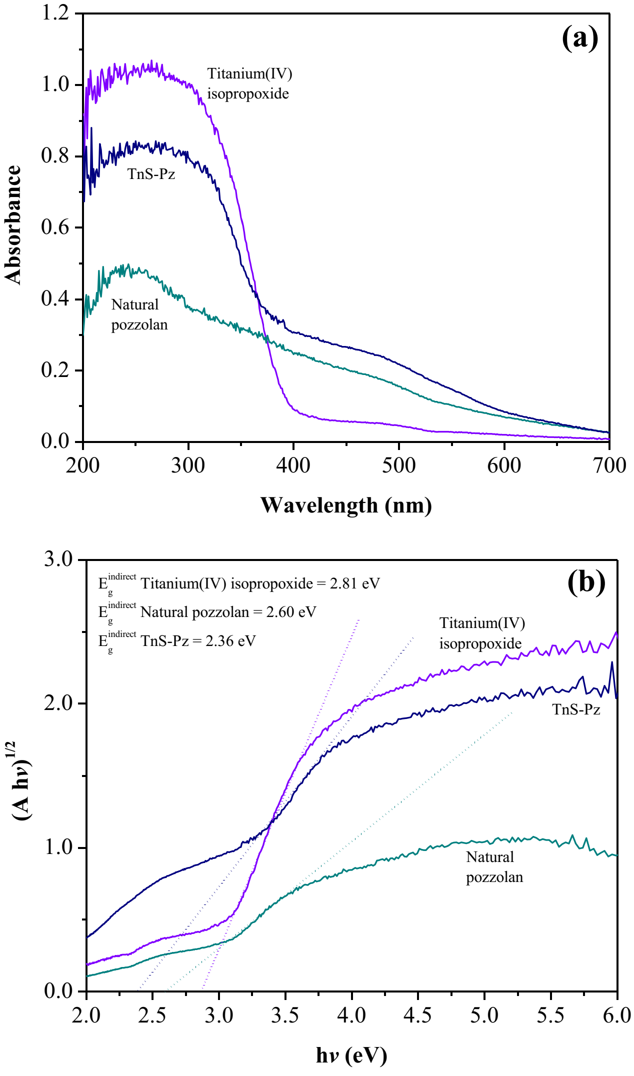

Fig. 2 **a** Diffuse reflectance of UV-Vis (DRUV) absorption spectra of natural pozzolan, hybrid material (TnS-Pz), and titanium(IV) isopropoxide, — titanium(IV) isopropoxide; — TnS-Pz; — Pz. **b** The indirect interband transition energies of the TnS-Pz samples. "A" in the label on the y-axis stands for absorbance, which is proportional to the absorption coefficient α. — titanium(IV) isopropoxide; — TnS-Pz; — Pz

Results and discussion

Characterization of the TnS-Pz sample

The nitrogen adsorption-desorption isotherm was performed to measure the specific surface area and understand the pore nature of the TnS-Pz material. As shown in Fig. 1, the TnS-Pz isotherm curve exhibited a curve type IV isotherm with a hysteresis loop, representing capillary condensation, as is typical for mesoporous materials. The mesoporosity of the TnS-Pz is highlighted by the high external surface area equal to 160.2 $m^2\ g^{-1}$ when compared with the micropore material surface area (61.5 $m^2\ g^{-1}$). The nitrogen adsorption isotherms confirm the presence of micropores where the low-pressure region ($P/P_0 < 0.1$) exhibits a rapid increase in the uptake of N_2 as the relative pressure is increased. Regarding specific surface areas (S_{BET}), the precursor (natural pozzolan) exhibited a very low S_{BET} equal to 13.2 $m^2\ g^{-1}$ (Celik et al. 2014); however, the final hybrid material presented well-developed porosity with higher $S_{BET,}$ 271.7 $m^2\ g^{-1}$.

As the reflectance spectra (DRUV) help to understand the photocatalytic properties of the materials, the UV-Vis spectra of the TnS-Pz hybrid material were compared with the pure pozzolan (Pz) and titanium(IV) isopropoxide (Fig. 2a). The TnS-Pz material spectra showed a higher absorption region, in the UV spectrum, as well as that the titanium(IV) isopropoxide displays a higher absorption intensity than the other materials. However, from 400 up to 650 nm (visible region), the hybrid material presents a small increase in the absorption intensity compared with the precursors, suggesting the TnS-Pz to be electronically unstable through the interactions between them. Since the pozzolan structure is mainly based on SiO_2 and Al_2O_3, the Si-O-Ti and Al-O-Ti covalent bonds between the pozzolan and titanium(IV) isopropoxide must occur over both structures during the sol-gel process (Wang et al. 2017), changing their characteristics.

The DRUV spectra yielded the estimated bandgap energies as presented in Fig. 2a. The relation between the absorption coefficient (α) and incident photon energy ($h\nu$) follows Eq. (1).

$$\alpha = \mathrm{B_i}\frac{(\mathrm{h}\nu - \mathrm{E_g})^2}{\lambda} \tag{1}$$

where B_i is the absorption constant for indirect transitions (Lei et al. 2014a). The plots of $(Ah\nu)^{1/2}$ versus $h\nu$ from the spectral data in Fig. 2a are presented in Fig. 2b. By extrapolating the linear section of the curve (the traced line in Fig. 2b), the material's bandgap may be indirectly estimated, where a bandgap of around 2.36 eV for hybrid material was calculated (TnS-Pz). Moreover, wherein bandgap energies lower than 3.00 eV correspond to visible-light absorption (Lei et al. 2014a), the bandgap energies of titanium(IV) isopropoxide and natural pozzolan were 2.81 and 2.60 eV, respectively.

FTIR was used to analyze the functional groups present in TnS-Pz and natural pozzolan, both of whose band assignments of both materials are displayed in Table 1. There is a higher number of vibrational bands recorded in the TnS-Pz material than in natural pozzolan, chiefly in 1826 to 2531 cm^{-1} spectrum. The intense bands located at 3433 and 3331 cm^{-1} are assignable to hydroxyl stretching and the outer surface hydroxyl vibration of the pozzolan and TnS-Pz (Huang et al. 2017a; Wamba et al. 2017; Zeitler and Brown 1957). Similarly, the broad bands located around 1013 and 1058 cm^{-1} may be assigned to the Si–O–Si stretching vibration present in the pozzolan and TnS-Pz, respectively. Nevertheless, while the bands at 2923 and 2977 cm^{-1} correspond to the stretching vibration of $–CH_2$ itself (Wamba et al. 2017), they are observed only in the natural pozzolan band at 958 cm^{-1}, as assigned to the Si–O–Ti vibration (Huang et al. 2017a; Zeitler and Brown 1957). This vibration is only found in the TnS-Pz sample. The observations also confirm the hybridization process.

A scanning electron microscope (SEM) (Fig. 3) was used to examine the morphologies of the natural pozzolan and TnS-Pz. Figure 3a shows the natural pozzolan structure, composed of irregular particle sizes and regular smooth surfaces lacking evident porosity, thereby accounting for the low S_{BET} (13.2 $m^2\ g^{-1}$). However, the SEM image from the TnS-Pz material (Fig. 3b) indicates a large number of uneven thin nanosheet shapes, explained by the significant increased porosity ($S_{BET} = 271.7\ m^2\ g^{-1}$). This modification might correlate to the chemical bond between the natural pozzolan and titanium(IV) isopropoxide (Si–O–

Table 1 The main FTIR vibrational bands in natural pozzolan and TnS-Pz. All assignments are based according to the literature [24, 28, 29]

FTIR band (cm^{-1})	Assignments
Natural pozzolan	
3433	OH functional group stretching and bending
2923, 2977	$-CH_2$vibration
1634	Asymmetric hydroxyl groups
1381	H–O–H bending band
1033	Stretch vibration of Si–O–Si
543	Stretching of functional groups of Si–O–Al
TnS-Pz	
3331	O–H stretch
2315, 2322	C–H asymmetric stretch
1638	Asymmetric carboxylate stretch
1058	Si–O–Si stretch vibration
958	Si–O–Ti vibration
555	Stretching of functional groups of Si–O–Al

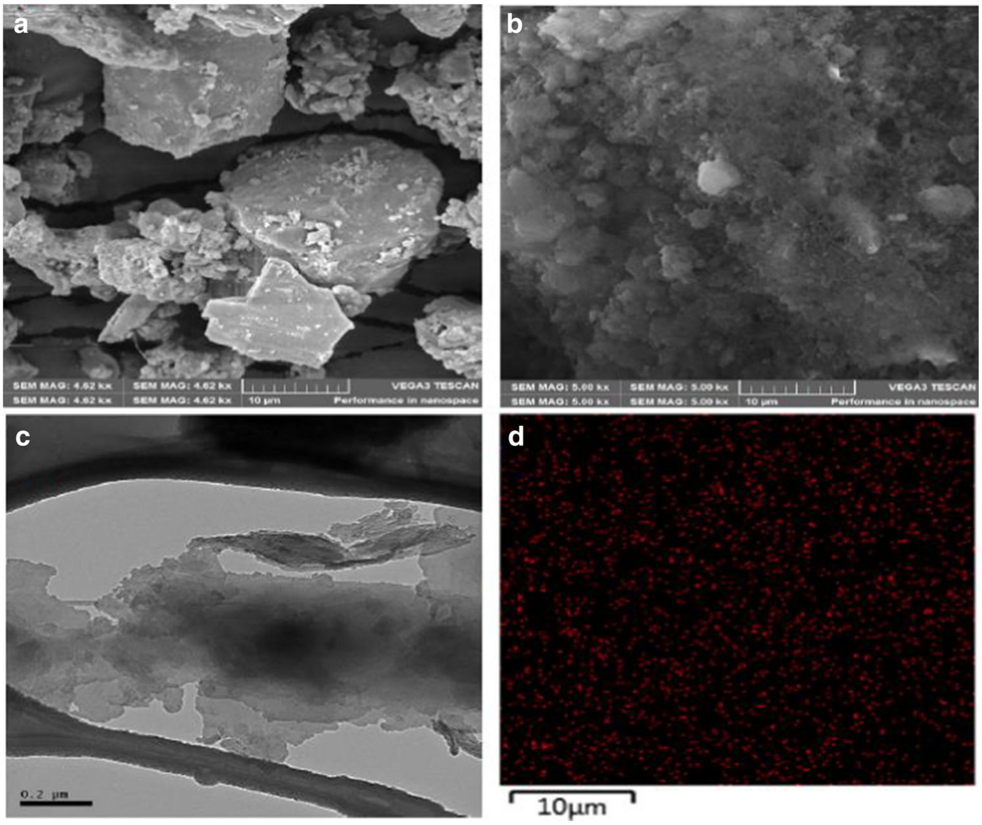

Fig. 3 **a**, **b** SEM images of pure pozzolan and TnS-Pz. **c** TEM images of pure pozzolan and TnS-Pz. **d** Chemical map for Ti-K energy

Ti and Al–O–Ti) in the hybridization process, as well as by the accumulation of Ti nanoparticles over the surface TnS-Pz in the formed nanosheets.

A TEM analysis was carried out for further morphologic investigation of the synthesized TnS-Pz (Fig. 3c), showing the morphology of the TnS-Pz where the agglomerated structures and nanoplatelets/nanosheets were a minimum of one direction lower than 100 nm in width size.

An energy-dispersive X-ray (EDX) was also used to further analyze the composition of TnS-Pz. The elemental map (Fig. 3d) confirms the presence of Ti particles covering the natural pozzolan and concurs with the proposed structure of the synthetized TnS-Pz.

In the XRD patterns of the TnS-Pz sample (Fig. S4), the main contribution originates from the diopside/diopside aluminian phase (88.7%) and its monoclinic structure containing a *C*2/*c* space group. The diopside is a member of the larger pyroxene group ($M2M1Si_2O_6$), where the cations may occupy the two non-equivalent sites of both M2 and M1. These sites' geometry depends on the composition and the space group of the pyroxene member (Biedermann et al. 2015; De Grave and Eeckhout Sigrid 2003; Dyar et al. 2013). The smaller M1 site is sixfold coordinated site—the octahedron is nearly regular and may be occupied by smaller cations (such as Mg^{2+}, Fe^{2+}, Fe^{3+}, Al^{3+}, or Ti^{4+}). The strongly irregular M2 site ranges from six (spodumene) to eightfold (diopside, augite, aergine) larger (Biedermann et al. 2015). The pyroxenes that crystallize in the monoclinic crystal system are clinopyroxenes; the Ca^{2+}-saturated *C*2/*c* end-members are diopside ($CaMgSi_2O_6$) and hedenbergite ($CaFeSi_2O_6$); as well, the intermediate *C*2/*c* solid solution is an augite (nominally (Ca, Na) (Mg, Fe, Al, Ti) $(Si,Al)_2O_6$). The Ca^{2+} has a strong preference for the larger M2 site in the synthetic diopside. In natural samples, the substitution of Ca by Na and Mg by Fe is common. When a larger M2 site is vacant, the Fe^{2+} ions prefer the M2 site; Fe^{2+} and Fe^{3+} are otherwise located in smaller M1 sites (Biedermann et al. 2015; De Grave and Eeckhout Sigrid 2003; Dyar et al. 2013).

The minor contribution in the XRD profiles of TnS-Pz sample corresponds to the $Ca(Al_2Si_2O_8)$ compound comprised of a hexagonal structure of titanium oxides (anatase, rutile), and iron (titanium) oxides (hematite and titanomagnetite). The titanomagnetites ($Fe_{3-x}Ti_xO_4$, $0 \leq x \leq 1$) are solid solutions of magnetite and ulvöspinel (Banerjee et al. 1967; Bowles et al. 2013; Hamdeh et al. 1999; Liu et al. 2014; M. Hassan and Dekan 2013; Sorescu et al. 2012; Tanaka and Kono 1987). The magnetite ($x = 0$, stoichiometric) has an inverse spinel crystal structure according to the formula $(Fe^{3+})^A(Fe^{3+}\ Fe^{2+})^B\ O^{2-}{}_4$. The A-sites (tetrahedral sites) are occupied by Fe^{3+} ions and the B-sites (octahedral sites) by the Fe^{3+} and Fe^{2+} ions. At temperatures above the Verwey transition temperature (~ 119 K), a rapid electron exchange occurs between the Fe^{2+} and Fe^{3+} ions at the B-sites where a mixed 2.5 + iron valence state is detected (Gunnlaugsson et al. 2008; Kündig and Steven Hargrove 1969; Sorescu et al. 2012). In

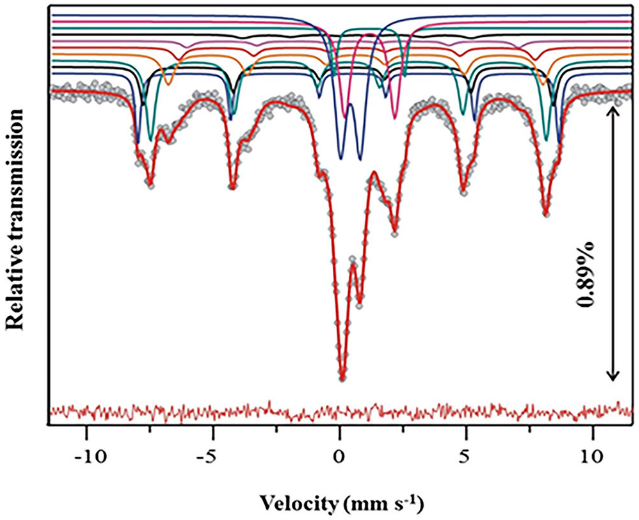

Fig. 4 The room temperature ^{57}Fe-Mössbauer spectra of the TnS-Pz sample. The solid circles represent the experimental data and the red solid line represents the corresponding fit. The fitted lines of the Mössbauer subspectra are plotted above the main spectrum fit—sextets D (blue), E (black), F (dark cyan), G (orange), H (red), J (magenta), and K (black); doublets A (dark cyan), B (pink), and C (blue). The vertical arrow denotes the relative position of the lowest peak with respect to the basal line. The red solid line in the lower area of the plot represents the error calculated as the difference (Fit-Exp). The largest value of the absolute difference is less than 0.08%

intermediate compositions that have a more complex spinel structure, Ti^{4+} ions replace some of the Fe^{3+} ions on the B-sites; therefore, in order to maintain charge neutrality, another Fe^{3+} ion at A- or B-site must convert to a Fe^{2+} ion. The other end member, ulvöspinel ($x = 1$), is also an inverse spinel, as presented by the formula $(Fe^{2+})^A$ $(Fe^{2+}\ Ti^{4+})^B$ $O^{2-}{}_4$ (Sorescu et al. 2012).

Due to the presence of these disparate phases in the sample where overlapping Mössbauer parameters occur, there is a consequent complex spectra fitted with several Mössbauer subspectra: doublets (two lines of the absorption feature) and sextets (six lines of the absorption feature). The ^{57}Fe-Mössbauer spectrum of the TnS-Pz sample is shown in Fig. 4, together with the total fit and a resolved subspectrum.

The fitted Mössbauer parameters of the subspectrum are presented in Table 2. Numerous initial attempts to fit the spectrum included several sextets, ferric and ferrous doublets, constrained and non-constrained. The initial number of components and fitting constraints was based on prior Mössbauer tests on the Fe-bearing phases present in the samples. As reported in the literature, for the central analyzed spectrum, one or two ferric doublets found for the anatase (Cordischi et al. 1985; Patel et al. 2012; Rodríguez-Torres et al. 2008; Zhu et al. 2005) and rutile (Balcells et al. 2006; Cabrera et al. 2006; Cordischi et al. 1985; Nozik 1972; Sandin et al. 1976; Stampel et al. 1973), two to five ferric and/or ferrous doublets for diopside (Biedermann et al. 2015; De Grave and Eeckhout Sigrid 2003; Dyar et al. 2013; J. G. Stevens 2005; Van Alboom et al. 1991) and augite (Biedermann et al. 2015; J. G. Stevens 2005; Whipple 1974) as well as for other members of the clinopyroxene group (Akasaka 1983; Biedermann et al. 2015; Eeckhout Sigrid and Grave 2003; J. G. Stevens 2005; Redhammer Günther et al. 2006) were considered to be fits. For the magnetic area, one sextet for the hematite (Dyar et al. 2006; J. G. Stevens 2005), two sextets for the magnetite (Dyar et al. 2006; J. G. Stevens 2005; Kündig and Steven Hargrove 1969; M. da Costa et al. 1995), and numerous other studies have detected multiple doublets and/or sextets for titanomagnetite (Banerjee et al. 1967; Bowles et al. 2013; Gattacceca et al. 2013; Hamdeh et al. 1999; J. Sitek 2013; Liu et al. 2014; M. Hassan and Dekan 2013; Morris et al. 1993; Sorescu et al. 2012; Tanaka and Kono 1987); as such, they were taken into account during the fitting procedure. To the best of the authors' knowledge, there are no reported Mössbauer parameters for the $Ca(Al_2Si_2O_8)$ compound containing a hexagonal structure as found in the TnS-Pz sample. Due to the origin of this phase as an intermediate phase in the

Table 2 Room temperature ^{57}Fe-Mössbauer hyperfine parameters for the TnS-Pz sample. A, the relative area of the Mössbauer subspectrum; Γ, line width (FWHM); δ, isomer shift; Δ, quadrupole splitting in a pure electric interaction; 2ε, the quadrupole shift in a combined strong magnetic and weak electric interaction; B_{hf}, the hyperfine magnetic field. The fitting errors are given in parenthesis

Mössbauer subspectrum TnS-Pz	A [%]	Γ [mms^{-1}]	Δ [mms^{-1}]	$\Delta/2\varepsilon$ [mms^{-1}]	B_{hf} [T]	Iron valence state
A-doublet	18 (1)	0.56 (1)	0.376 (4)	0.778 (7)		Fe^{3+}
B-doublet	11 (2)	0.52 (2)	1.146 (5)	1.98 (1)		Fe^{2+}
C-doublet	2 (1)	0.24 (5)	1.14 (1)	2.79 (3)		Fe^{2+}
D-sextet	7 (2)	0.24 (4)	0.380 (7)	− 0.17 (1)	51.66 (9)	Fe^{3+}
E-sextet	8 (4)	0.36 (8)	0.37 (1)	− 0.15 (2)	50.3 (2)	Fe^{3+}
F-sextet	24 (3)	0.42 (3)	0.300 (5)	0	48.55 (7)	Fe^{3+}
G-sextet	16 (4)	0.54 (7)	0.59 (1)	0	46.0 (2)	$Fe^{2.5+}$
H-sextet	6 (4)	0.5 (2)	0.64 (3)	0	43.8 (4)	$Fe^{2.5+}$
J-sextet	4 (2)	0.6 (2)	0.48 (5)	0	40.7 (4)	$Fe^{2.5+}$
K-sextet	4 (1)	0.8 (2)	0.63 (8)	0	28.0 (6)	$Fe^{2.5+}$

thermal transformation of the Ca-LTA zeolite structure into anorthite (Dimitrijević et al. 1996), the measured spectrum may contain ferric and/or ferrous doublets related to this phase resembling those found for other aluminosilicate phases (J. G. Stevens 2005).

Based on the features seen in the fits made incorporating and not incorporating constraints, two key decisions were made after the preliminary fits. The first distinctive attribute was observed for the central section of TnS-Pz spectrum. Due to the overlapping of the Mössbauer lower velocity absorption lines for the ferric and ferrous doublets corresponding to the anatase, rutile, high titanomagnetite, diopside, and augite as well as to the hexagonal $Ca(Al_2Si_2O_8)$ phase, the initial larger number of doublets decreased to only five constrained ones that could be fairly resolved. The constraints imposed were the same line width (FWHM) for the ferric and the same FWHM for the ferrous doublets. The larger number of doublets of imposed constraints neither pointed to any specific pairs of doublets for the abovementioned phases nor provided any reasonable assignments to the observed phases. Therefore, all constraints for the central section of the final fits were lifted. A limited number of the initial doublets merged after lifting; hence, only three doublets in total could be retained in the final fits. Important features in the measured spectrum were also found for the magnetic section at the ambient temperature. There were highly characteristic of spectral features, two sextets with $B_{hf} \sim 49$ T; $\delta \sim 0.3$ mms^{-1} and $B_{hf} \sim 46$ T; $\delta \sim 0.63$ mms^{-1}, which generally correspond to the magnetite phase for the A- and B-sites, respectively. These are yet also of the ratio of relative subspectrum areas 2:1 instead of 1:2 (Kündig and Steven Hargrove 1969; M. da Costa et al. 1995). The sizeable line width of the A-site sextet was recorded as well. One interpretation of these lines is that there may be another phase or more phases that contribute to the A-site sextet of the $B_{hf} \sim 49$ T in addition to the magnetite phase (Gunnlaugsson et al. 2006; Gunnlaugsson et al. 2003). As the oxidation of titanomagnetite to titanomaghemite (i.e., the "maghemitization" process) is commonly found in nature (de Oliveira et al. 2002; Tanaka and Kono 1987; Xu et al. 1997), the titanomaghemite phase was also taken into account for the evaluation of TnS-Pz spectrum. Other research into titanomagnetite (M. Hassan and Dekan 2013; Sorescu et al. 2012; Tanaka and Kono 1987) has noted the appearance of one or two new sextets accompanied by the simultaneously lowering of hyperfine magnetic fields. Moreover, the broadening of A- and B-site sextets was also been noted with an increase of Ti content in the Ti-doped magnetite phase. More sextets were added to the area of the $B_{hf} \sim 49$ T sextet, whereby the range of $B_{hf} \sim 48$–52 T described the final fit of three sextets. Moreover, for the TnS-Pz sample, following the preliminary fits, magnetic components were observed below the $B_{hf} \sim 48$ T that reached nearly zero quadrupole shifts. These shifts were set to zero in the final fit (Table 2). As regards interpreting the TnS-Pz spectrum in the $B_{hf} \sim 47$–52 T range, the fully oxidized magnetite—i.e., the maghemite phase $(Fe^{3+})^A\ (Fe^{3+}_{5/3}\square_{1/3})^B\ O^{2-}_4$ that is also an inverse spinel (□ denote vacancy)—lacks Fe^{2+} ions in the structure. This fact was also taken into consideration. Since the A- and B-site sextets had approximate values of the hyperfine magnetic fields, only one sextet of $B_{hf} \sim 50$ T ($\delta \sim 0.32$ mms^{-1}) was found in the maghemite spectrum at room temperature (Dyar et al. 2006; J. G. Stevens 2005). Partially oxidized magnetite or the mixture of magnetite and maghemite is able to contribute to the spectra within the same range of a hyperfine parameter (Fock et al. 2017; Joos et al. 2016). The non-stoichiometric $Fe_{3\text{-}x}O_4$ contains vacancies presumably on the B-sites in relation to the amount of the Fe^{2+} in the magnetite structure (A. Gorski and Scherer 2010; Kalska-Szostko et al. 2015) and may have been formed in the sample. From an experimental point of view, since stoichiometric/non-stoichiometric magnetite and maghemite have quite similar inverse spinel structures, it is often difficult to distinguish between the two crystallographic structures or their mixtures since X-ray diffraction is less sensitive than the Mössbauer technique (Fock et al. 2017). In addition to the Ti^{4+} ions, impurity ions such as Al^{3+}, Ca^{2+}, Mg^{2+}, and Si^{4+} can be substituted for Fe^{3+} ions in hematite and maghemite. These impurities contribute to chemical and structural disorder in the crystal structure, leading to additional sextets or distributions of hyperfine magnetic fields in the Mössbauer spectra. Similar distributions can be found for natural (titano)magnetite samples, where the same impurity ions commonly substitute Fe^{3+} and/or Fe^{2+} (Bowles et al. 2013). Therefore, for the evaluation of TnS-Pz spectrum, the Mössbauer parameters for the doped hematite, magnetite, and maghemite phases were also considered.

The assignment of the Mössbauer subspectrum presented in Table 2 was done as follows: the Fe^{3+} D-sextets for the TnS-Pz sample belong to the hematite/titanohematite phase (Dyar et al. 2006; J. G. Stevens 2005; McEnroe et al. 2016). The titanohematites are solid solutions between the two end-members of hematite (α-Fe_2O_3) and ilmenite ($FeTiO_3$) (McEnroe et al. 2001). The formation of a titanohematite phase must be taken into consideration due to the presence of Ti^{4+} ions embedded in the titanium(IV) isopropoxide starting material used to produce the TnS-Pz sample. While the Fe^{3+} E-sextets dominantly originate from the titanohematite phase (McEnroe et al. 2016), minor contributions from the maghemite (J. G. Stevens 2005) and titanomagnetite cannot be entirely excluded (McCammon et al. 1999; Sorescu et al. 2012). The titanomagnetites contributed to the F–J-sextets, where a substantial range of hyperfine magnetic fields ($B_{hf} \sim 40$–52 T) and considerable line widths were all recorded. As such, this does indicate that either more than one titanomagnetite phase (Sorescu et al. 2012; Tanaka and Kono 1987) coupled by a non-stoichiometric magnetite may contribute to these sextets or that additional doped hematite (McEnroe et al. 2016) and pure/doped maghemite (Allan et al. 1988; J. G. Stevens 2005; Xu et al. 1997) do so as well. For the TnS-Pz sample, the titanomaghemite may contribute substantially to the sextet due to the fact that the F-sextet exhibited a pure Fe^{3+} character (Chevrier et al. 2006). The very broad K-sextet may be ascribed only to the titanomagnetites (Sorescu et al. 2012), but the pyrrhotite phase was unable to be excluded from the results of the Mössbauer investigation (Gattacceca et al. 2013). The G–K-sextets with the $Fe^{2.5+}$ characters indicate Fe-Ti spinel-type phases similar to the magnetite structure of the electron hopping between the octahedral sites.

The three doublets located in the central section of the spectrum partially originate from the dominant diopside/diopside aluminum phase. Similar Mössbauer parameters for the Fe^{3+} A-doublet were found for the diopside (De Grave and Eeckhout Sigrid 2003; McCanta and Dyar 2017) where the ferric ions usually prefer the M1 site in the pyroxenes. Since it is not commonly found for diopsides (Dyar et al. 2006; J. G. Stevens 2005), a similar doublet was described in a more general manner as Fe^{3+} in the pyroxenes (Chevrier et al. 2006; Gunnlaugsson et al. 2006; Gunnlaugsson et al. 2003) or as Fe^{3+} at the M1 site in the clinopyroxene (Akasaka 1983; Dyar et al. 1989). One possible reason for the A-doublet's major broadening is that it is unable to be assigned solely to one specific phase. Ferric ions embedded in titan oxides also contribute to the same absorption area in the TnS-Pz spectrum (Balcells et al. 2006; Cabrera et al. 2006; Nozik 1972; Patel et al. 2012; Sandin et al. 1976; Stampel et al. 1973; Zhu et al. 2005). The A-doublet may be partially associated with the various superparamagnetic iron oxide/iron hydroxide nanoparticles (smaller than 10–15 nm), which are not easily distinguishable in the Mössbauer spectrum at ambient temperatures (Joos et al. 2016). The Fe^{2+} B-doublet and Fe^{2+} C-doublet dominantly belong to the diopside/diopside aluminum phase, where ferrous ions are most likely positioned at the M2 and M1 sites, respectively. Verifying the assignment, similar doublets for the Fe^{2+} at the M2 and M1 sites were found for the titanaugite (Whipple 1974) and clinopyroxene (Dyar et al. 1989; Dyar et al. 2013). At a minimum, the minor contributions of the high timagnetites (Sorescu et al. 2012) to the Fe^{2+} paramagnetic section of the TnS-Pz spectrum would be covered by the clinopyroxene's doublets.

Only an estimate may be given that iron ions, such as (titano)magnetites and (titano)hematite, are embedded more in the magnetic phases present in the Fe-bearing phases present in the sample.

Cr(VI) photoreduction studies

The photocatalytic activity of the TnS-Pz was evaluated through the photoreduction of 0.2 mM of Cr(VI) under UVA-Vis radiation. The experiments were performed in the presence of citric acid as a sacrificial agent in a 3:1 $[scavenger]_0/[Cr(VI)]_0$ M ratio, with a catalyst load of 15 mg L^{-1}, pH 3.0, and 25 °C. The preliminary tests showed that the Cr(VI) reduction was negligible after 180 min under UVA-Vis radiation in the absence of catalyst where there was no addition of sacrificial agents (Fig. S5). Likewise, the same behavior was observed in the system with Cr(VI) in presence of only citric acid (Fig. S5). The slight (10%) Cr(VI) photocatalytic reduction observed in the absence of scavenging agents after 180 min of irradiation (Fig. S5) may be chiefly attributed to a short circuiting caused by the continuous reduction and reoxidation of chromium species by holes or hydroxyl radicals when the scavenger agent is not present in the system (Marinho et al. 2017b). The reaction in the presence of citric acid and UVA-Vis (absent of catalysts) leads to a Cr(VI) reduction of 30% in 180 min, whose behavior is explainable by the citric acid oxidation through the photo-induced electron transfer (PET) that acts as electron donor (Mytych and Stasicka 2004).

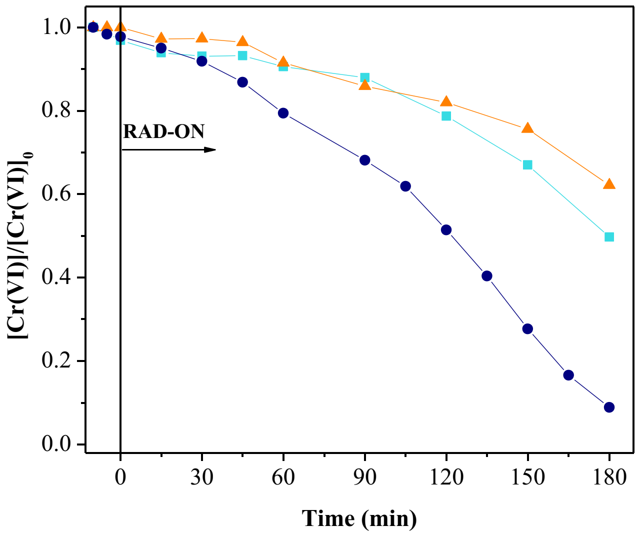

Fig. 5 Cr(VI) photoreduction over different photocatalysts. (▲) TiO_2-P25/citric acid/UVA-Vis, (■) TnS/citric acid/UVA-Vis, (●) TnS-PZ/citric acid/UVA-Vis. $[Cr(VI)]_0 = 0.2$ mM; catalyst loading = 15 mg L^{-1}; $[citric\ acid]_0/[Cr(VI)]_0$ M ratio = 3:1; pH = 3.0; and 25 °C

In order to compare the effectiveness of the titanium(IV) isopropoxide/pozzolan nanosheets (TnS-Pz) in the Cr(VI) photoreduction, the reaction with titanium(IV) isopropoxide nanosheets (TnS) and pure TiO_2-P25 was assessed (Fig. 5). The TnS-Pz presented a higher efficiency in the Cr(VI) reduction than the pure TiO_2-P25. Moreover, in the TnS-Pz/citric acid/UVA-Vis system, the initial Cr(VI) concentration almost reached complete diminishment after 150 min. However, in its reaction with pure TiO_2 (TiO_2-P25/citric acid/UVA-Vis system), only 21% of Cr(VI) reduced during the same reaction time. In addition, a tenfold increase on the photocatalytic reduction rate (pseudo first-order kinetic) was found when using

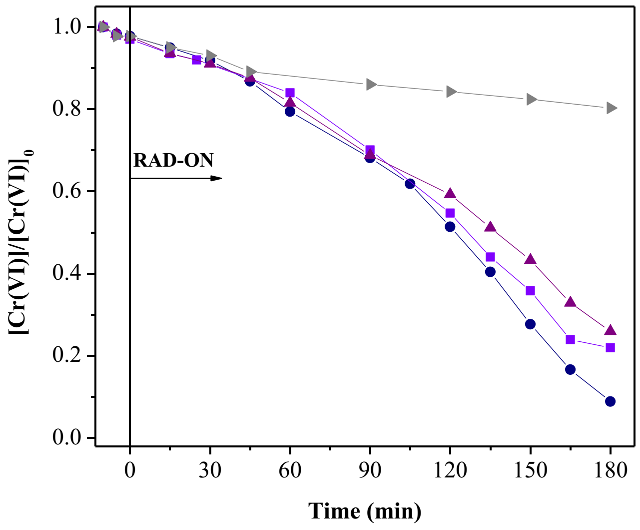

Fig. 6 The influence of pH on the photocatalytic reduction of Cr(VI) in the TnS-Pz/UVA-Vis/citric acid system at 25 °C. $[Cr(VI)]_0 = 0.2$ mM; catalyst loading = 15 mg L^{-1}; $[citric\ acid]_0/[Cr(VI)]_0$ M ratio = 3:1; pH: (●) 3.0, (■) 4.0, (▲) 5.0, (▶) 6.0

TnS-Pz ($k = 11 \times 10^{-3}$ min^{-1}) as a photocatalyst when compared with the TiO_2-P25 ($k = 1.1 \times 10^{-3}$ min^{-1}) (Table S1).

Owing to the fact that the system's radiation source emits up to 440 nm (Fig. S3), the better efficiency of the TnS-Pz may be attributed to the DRUV analysis of the catalyst as well as that the indirect bandgap energy determined was the lowest ($E_g{}^{indirect}{}_{TnS\text{-}Pz} = 2.36$ eV). The TiO_2-P25 demonstrated no satisfactory results under the UVA-Vis, presenting an indirect bandgap value of 3.10 eV (Guayaquil et al. 2017) that is higher than the synthesized hybrid material.

It is important to note that the Cr(total) concentration remained constant (data not shown) in all experiments, thereby indicating no chromium(III) adsorption on the catalyst's surface.

The effect of pH on the photocatalytic reduction of the Cr(VI) by TnS-Pz/UVA-Vis/citric acid system

The solution pH is crucial to the Cr(VI) reduction in the photocatalytic system with TiO_2 (Marinho et al. 2017a; Marinho et al. 2017b). Nevertheless, in order to verify the influence of pH on the TnS-Pz/UVA-Vis/citric acid system, a set of reduction experiments were carried out with 0.2 mM of the Cr(VI), $[citric\ acid]_0/[Cr(VI)]_0$ M ratio = 3:1, 25 °C, varying the pH from 3.0 to 6.0 (Fig. 6). The results shown in Fig. 6 and Table S1 present that, as the pH increases, the reaction rate also substantially decreases. This respective reaction demonstrates that the pH plays a significant role in Cr(VI) reduction. In the pH 3.0 system, a complete reduction (below the detection limit) was achieved in 180 min, while for the pH 4.0 and 5.0, the reduction achieved was roughly 75% over the same time, and the pH 6.0 reaction reduced less than 20% of the Cr(VI). The kinetic constant presented the same behavior, decreasing from 11×10^{-3} to 1.3×10^{-3} min^{-1} when the pH was increased from 3.0 to 6.0, respectively. These results may stem from the global reduction reaction, which consumes protons and is also favored at lower pH values (Marinho et al. 2016).

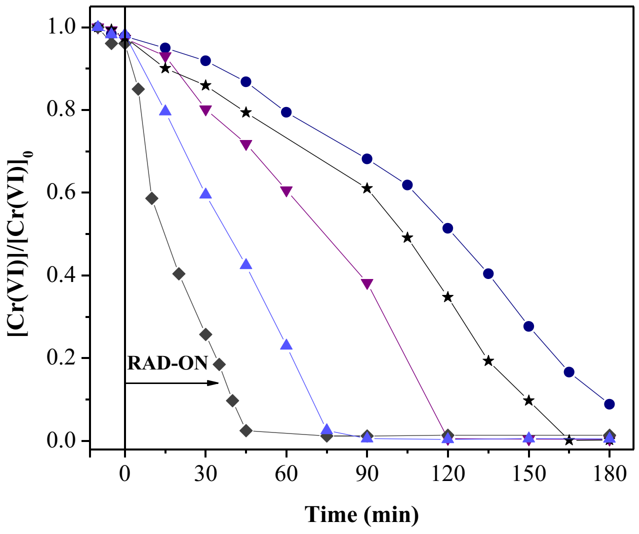

Fig. 7 The influence of the initial Cr (VI) concentration on the photocatalytic reduction in the TnS-PZ/UVA-Vis/citric acid system at pH 3.0 and 25 °C. Catalyst loading = 15 mg L^{-1}; $[citric\ acid]_0/[Cr(VI)]_0$ M ratio = 3:1; $[Cr\ (VI)]_0$: (●) 0.20 mM, (★) 0.15 mM, (▼) 0.10 mM (▲), 0.04 mM, (◆) 0.02 mM

The effect of the initial concentration of Cr(VI) on the photocatalytic reduction of Cr(VI) by the TnS-Pz/UVA-Vis/citric acid system

The effect of the initial Cr(VI) concentration on its photoreduction was evaluated by varying the corresponding concentration from 0.02 to 0.20 mM at pH 3.0 and 25 °C where the citric acid was proportional at a 3:1 $[citric\ acid]_0$:$[Cr(VI)]_0$ M ratio. As depicted in Fig. 7, the Cr(VI) reduction's efficiency gradually decreases while matching the increase of the respective initial concentration. For the lowest concentrations studied (0.02 mM), a total reduction of Cr(VI) was achieved after a reaction time of 45 min. However, for the initial concentrations of the Cr(VI) (0.20 mM), approximately 95% of reduction was achieved in 180 min.

Accompanied by the tenfold increase of the initial concentration of Cr(VI) from 0.02 to 0.20 mM, Table S1 shows that the reaction rate decreased approximately 5-fold ($k = 52 \times 10^{-3}$ and $k = 11 \times 10^{-3}$ min^{-1}). Such behavior has been recorded in other studies on TiO_2-P25 in suspension (Ku and Jung 2001) and verified (Marinho et al. 2017a), where the initial concentration of Cr(VI) is tripled, causing a 3 to 13-fold reduction in the reaction rate times. The negative effect of higher concentrations of Cr(VI) can be attributed to the surface's saturation of the catalyst by the Cr(VI) species, thereby

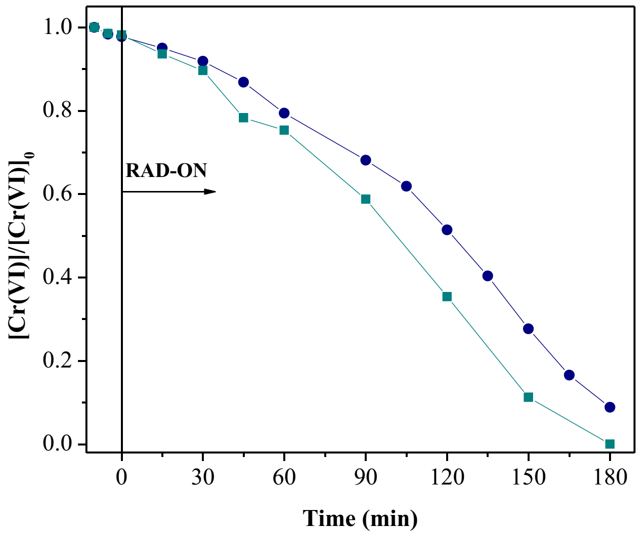

Fig. 8 The influence of scavenger type on the photocatalytic reduction of Cr (VI) in the TnS-PZ/UVA-Vis system at pH 3.0 and 25 °C. $[Cr (VI)]_0 = 0.20$ mM, catalyst loading = 15 mg L^{-1}; $[scavenger]_0/[Cr(VI)]_0$ M ratio = 3:1; scavenger: (●) citric acid, (■) tartaric acid

preventing the binding of the citric acid species, as similar effects have been reported previously by Chakrabarti et al. (2009) and Valari et al. (2015). In addition, the competition between the Cr(VI) and the citric acid species may occur for the binding sites on the surface of the catalyst, generating a screen effect, where the Cr(VI) is able to impede light entry onto the surface of the catalyst (TnS-Pz), which, in response, decreases the photocatalytic reduction efficiency of Cr(VI).

The effect of the scavenger (by type) on the photocatalytic reduction of Cr(VI) by the TnS-Pz/UVA-Vis system

The photocatalytic Cr(VI) reduction by TiO_2 was reported to be enhanced through the addition of tartaric acid as sacrificial agents (Marinho et al. 2017b). Therefore, this scavenging agent was tested on a Cr(VI) (0.2 mM) reduction using the TnS-Pz/UVA-Vis system (15 mg L^{-1} of TnS-Pz, at pH 3.0 and 25 °C).

As presented in Fig. 8, the results using both scavenger agents were similar as they attained a total Cr(VI) reduction (below the D_L of the method) after 180 min of reaction time.

These similar results likely stem from the organic acids being able to oxidize in the catalytic system, resulting in the formation of highly reduced radicals (such as $HCOO^{\bullet -}$). The ability also allows for an indirect radical-mediated reaction in the solution bulk, thereby intensifying the Cr(VI) reduction.

In the heterogeneous photocatalysis using TiO_2, the better efficiency of the tartaric acid systems may be explained by the higher energy of the highest occupied molecular orbital (E_{HOMO}) and the lower adiabatic ionization potential (AIP) of the tartaric acid as it favors the electron transfer within the TiO_2 organic acid complex (Wang et al. 2010). However, these thermodynamic driven forces do not appear to be essential in the TnS-Pz/UVA-Vis system.

Conclusion

This work presents the synthetization of a new hybrid material by the sol-gel process using natural pozzolan and titanium(IV) isopropoxide as precursors. Ti–O–Si and Ti–O–Al covalent bonds between the titanium(IV) isopropoxide and pozzolan are shown to be formed during the sol-gel process yielding the hybrid material. The surface area was found to be 271.7 m^2 g^{-1} and of a mesoporous structure. The morphology studies (SEM and TEM) showed that the material presents a hybrid nanosheet structure. The ultraviolet-visible diffuse reflectance (DRUV) absorption detected a varied electronic structure of the material whose material bandgap was estimated as 2.36 eV, which confirms the hybridization process. Comprehensive structural analysis (XRD) has shown the main mineral constituents of hybrid material (Al/Si/Fe/Ti oxides) and confirmed that structural properties—the chemical states on the activated surface sites (MB)—determined their affinity of forming hydroxyl agents.

The Cr(VI) reduction was successfully achieved with the TnS-Pz hybrid material, in the presence of hole/hydroxyl radical scavenger and UVA-Vis radiation. When optimized, a complete 0.2 mM Cr(VI) reduction was achieved after 180 min of reaction time in the presence of a 15 mg L^{-1} catalyst load, $[tartaric\ acid]_0/[Cr(VI)]_0$ M ratio = 3:1, pH 3, and 25 °C under UVA-Vis radiation.

Acknowledgments The authors would like to acknowledge LABMASSA – Mass Transfer Laboratory of the Federal University of Santa Catarina (UFSC), the supplier of all laboratory infrastructure used in this research project. Aline M. Novack acknowledges her scholarship supported by CAPES. Dr. Glaydson Simoes dos Reis is grateful to the Council for the Development of Higher Education at the Graduate Level, Brazil (CAPES) for his postdoctoral scholarship granted through National Postdoctoral Program (PNPD). Maja Đolić acknowledges the grant from the Ministry of Education and Science of the Republic of Serbia (III 43009). Vítor J.P. Vilar acknowledges the 2017 FCT Individual Call to Scientific Employment Stimulus (CEECIND/01317/2017).

Funding information This work was financially supported by CAPES-PRINT, project number 88887.310560/2018-00, and Associate

Laboratory LSRE-LCM - UIDB/50020/2020—funded by national funds through FCT/MCTES (PIDDAC).

References

A. Gorski C, Scherer M (2010): Determination of nanoparticulate magnetite stoichiometry by Mossbauer spectroscopy, acidic dissolution, and powder X-ray diffraction: a critical review vol 95

Adán C, Bahamonde A, Fernández-García M, Martínez-Arias A (2007) Structure and activity of nanosized iron-doped anatase TiO_2 catalysts for phenol photocatalytic degradation. Appl Catal B Environ 72:11–17

Akasaka M (1983) 57Fe mössbauer study of clinopyroxenes in the join CaFe3+ $AlSiO_6$ - $CaTiAl_2O_6$. Phys Chem Miner 9:205–211

Allan J, Coey JMD, Resende M, Fabris J (1988): Magnetic properties of iron-rich oxisols vol 15

Avansi W, Arenal R, de Mendonça VR, Ribeiro C, Longo E (2014) Vanadium-doped TiO_2 anatase nanostructures: the role of V in solid solution formation and its effect on the optical properties. Cryst Eng Comm 16:5021–5021

Balcells L, Frontera C, Sandiumenge F, Roig A, Martínez B, Kouam J, Monty C (2006) Absence of ferromagnetism in Fe-doped TiO_2 nanoparticles. Appl Phys Lett 89:122501

Banerjee SK, O'Reilly W, Gibb TC, Greenwood NN (1967) The behaviour of ferrous ions in iron-titanium spinels. J Phys Chem Solids 28: 1323–1335

Biedermann AR, Pettke T, Bender Koch C, Hirt AM (2015): Magnetic anisotropy in clinopyroxene and orthopyroxene single crystals Journal of Geophysical Research: Solid Earth 120, 1431–1451

Bowles J, Jackson M, Berquo T, Sølheid A P, Gee S J (2013): Inferred time- and temperature-dependent cation ordering in natural titanomagnetites vol 4

Brand R (2008) WinNormos Mössbauer Fitting Program. Universität Duisburg, Duisburg

Byrne C, Subramanian G, Pillai SC (2017) Recent advances in photocatalysis for environmental applications. Journal of Environmental Chemical Engineering 6:3531

Cabrera A, Rodriguez Torres C, Errico L, Sánchez FH (2006): Study of Fe-doped rutile TiO2 alloys obtained by mechanical alloying vol 384

Carolin CF, Kumar PS, Saravanan A, Joshiba GJ, Naushad M (2017) Efficient techniques for the removal of toxic heavy metals from aquatic environment: a review. Journal of Environmental Chemical Engineering 5:2782–2799

Celik K, Jackson M, Meral Akgul C, Emwas A-H, Mancio M, Mehta P, Monteiro P (2014) High-volume natural volcanic pozzolan and limestone powder as partial replacements for portland cement in self-compacting and sustainable concrete. Cem Concr Compos 45: 136–147

Chakrabarti S, Chaudhuri B, Bhattacharjee S, Ray AK, Dutta BK (2009): Photo-reduction of hexavalent chromium in aqueous solution in the presence of zinc oxide as semiconductor catalyst Chem Eng J 153, 86–93

Chevrier V, Mathe PE, Rochette P, Gunnlaugsson H (2006): Magnetic study of an Antarctic weathering profile on basalt: Implications for recent weathering on Mars vol 244

Choi W, Ko JY, Park H, Chung JS (2001) Investigation on TiO_2-coated optical fibers for gas-phase photocatalytic oxidation of acetone. Appl Catal B Environ 31:209–220

Cordischi D, Burriesci N, D'Alba F, Petrera M, Polizzotti G, Schiavello M (1985) Structural characterization of Fe/Ti oxide photocatalysts by X-ray, ESR, and Mössbauer methods. J Solid State Chem 56: 182–190

De Grave E, Eeckhout Sigrid G (2003): 57Fe Mössbauer-effect studies of Ca-rich, Fe-bearing clinopyroxenes: part III. Diopside vol 88

de Oliveira MTG, Formoso MLL, da Costa MI, Meunier A (2002) The titanomagnetite to titanomaghemite conversion in a weathered basalt profile from southern Paraná Basin, Brazil. Clay Clay Miner 50: 478–493

Dimitrijević R, Dondur V, Kremenović A (1996) Thermally induced phase transformations of Ca-exchanged LTA and FAU zeolite frameworks: Rietveld refinement of the hexagonal $CaAl_2Si_2O_8$ diphyllosilicate structure. Zeolites 16:294–300

Dong H, Zeng G, Tang L, Fan C, Zhang C, He X, He Y (2015) An overview on limitations of TiO_2-based particles for photocatalytic degradation of organic pollutants and the corresponding countermeasures. Water Res 79:128–146

Dyar M, McGuire AV, Ziegler RD (1989): Redox equilibria and crystal chemistry of coexisting minerals from spinel lherzolite mantle xenoliths vol 74

Dyar MD, Agresti DG, Schaefer MW, Grant CA, Sklute EC (2006) Mössbauer spectroscopy of earth and planetary materials. Annu Rev Earth Planet Sci 34:83–125

Dyar MD, Klima Rachel L, Fleagle A, Peel Samantha E (2013): Fundamental Mössbauer parameters of synthetic Ca-Mg-Fe pyroxenes vol 98

Eeckhout Sigrid G, Grave E (2003): 57Fe Mössbauer-effect studies of Ca-rich, Fe-bearing clinopyroxenes: part I. Paramagnetic spectra of magnesian hedenbergite vol 88

El Mragui A, Daou I, Zegaoui O (2019) Influence of the preparation method and ZnO/(ZnO + TiO_2) weight ratio on the physicochemical and photocatalytic properties of ZnO-TiO2 nanomaterials. Catal Today 321-322:41–51

Enuneku A, Biose E, Ezemonye L (2017) Levels, distribution, characterization and ecological risk assessment of heavy metals in road side soils and earthworms from urban high traffic areas in Benin metropolis, Southern Nigeria. Journal of Environmental Chemical Engineering 5:2773–2781

Eskandarloo H, Badiei A, Behnajady MA, Ziarani GM (2015) UV-LEDs assisted preparation of silver deposited TiO_2 catalyst bed inside microchannels as a high efficiency microphotoreactor for cleaning polluted water. Chem Eng J 270:158–167

Fock J et al. (2017): On the 'centre of gravity' method for measuring the composition of magnetite/maghemite mixtures, or the stoichiometry of magnetite-maghemite solid solutions, via 57Fe Mössbauer spectroscopy vol 50

Gattacceca J et al (2013) Opaque minerals, magnetic properties, and paleomagnetism of the Tissint Martian meteorite. Meteorit Planet Sci 48:1919–1936

Gholami M, Shirzad-Siboni M, Yang J-K (2016) Application of Ni-doped ZnO rods for the degradation of an azo dye from aqueous solutions. Korean J Chem Eng 33:812–822

Guayaquil F, Serrano Rosales B, Valades-Pelayo P, Lasa H (2017) Photocatalytic hydrogen production using mesoporous TiO_2 doped with Pt. Appl Catal B Environ 211:337

Gunnlaugsson H et al. (2003): Magnetic anomalies in Iceland: implications for the magnetic anomalies on Mars

Gunnlaugsson H, Helgason Ö, Kristjansson L, Nørnberg P, Rasmussen H, Steinþórsson S, Weyer G (2006): Magnetic properties of olivine basalt: application to Mars vol 154

Gunnlaugsson HP, Rasmussen H, Kristjánsson L, Steinthorsson S, Helgason Ö, Nørnberg P, Madsen MB, Mørup S (2008) Mössbauer spectroscopy of magnetic minerals in basalt on Earth and Mars. Hyperfine Interactions 182:87–101

Hamdeh H, Barghout K, Ho J-C, Shand P, Miller L. L (1999): A Mössbauer evaluation of cation distribution in titanomagnetites vol 191

Huang F, Tahmasbi Rad A, Zheng W, Nieh MP, Cornelius CJ (2017a) Hybrid organic-inorganic 6FDA-6pFDA and multi-block 6FDA-

DABA polyimide SiO_2–TiO_2 nanocomposites: synthesis, FFV, FTIR, swelling, stability, and X-ray scattering. Polymer 108:105–120

Huang H, Zhang J, Jiang L, Zang Z (2017b) Preparation of cubic Cu_2O nanoparticles wrapped by reduced graphene oxide for the efficient removal of rhodamine B. J Alloys Compd 718:112–115

Joos A, Rümenapp C, Wagner FE, Gleich B (2016) Characterisation of iron oxide nanoparticles by Mössbauer spectroscopy at ambient temperature. J Magn Magn Mater 399:123–129

Kalska-Szostko B, Satuła D, Olszewski W (2015) Mössbauer spectroscopy studies of the magnetic properties of ferrite nanoparticles. Curr Appl Phys 15:226–231

Khedr TM, El-Sheikh SM, Hakki A, Ismail AA, Badawy WA, Bahnemann DW (2017) Highly active non-metals doped mixed-phase TiO_2 for photocatalytic oxidation of ibuprofen under visible light. J Photochem Photobiol A Chem 346:530–540

Ku Y, Jung I-L (2001) Photocatalytic reduction of Cr(VI) in aqueous solutions by UV irradiation with the presence of titanium dioxide. Water Res 35:135–142

Kuhn HJ, Braslavsky SE, Schmidt R (2004): Chemical actinometry (IUPAC Technical Report) vol 76

Kumar K, Chowdhury A (2018): Use of novel nanostructured photocatalysts for the environmental sustainability of wastewater treatments. In: Reference module in materials science and materials engineering. Elsevier

Kündig W, Steven Hargrove R (1969) Electron hopping in magnetite. Solid State Commun 7:223–227

Lackhoff M, Prieto X, Nestle N, Dehn F, Niessner R (2003) Photocatalytic activity of semiconductor-modified cement-influence of semiconductor type and cement ageing. Appl Catal B Environ 43:205–216

Lei XF, Xue XX, Yang H (2014a) Preparation and characterization of Ag-doped TiO_2 nanomaterials and their photocatalytic reduction of Cr(VI) under visible light. Appl Surf Sci 321:396–403

Lei XF, Xue XX, Yang H (2014b) Preparation and characterization of Ag-doped TiO2nanomaterials and their photocatalytic reduction of Cr(VI) under visible light. Appl Surf Sci 321:396–403

Litter M (2015): Mechanisms of removal of heavy metals and arsenic from water by TiO_2-heterogeneous photocatalysis Pure and Applied Chemistry

Liu X et al. (2014): Structural and magnetic properties of Fe_2 TiO_4 Fe_3O_4 vol 50

M. da Costa G, De Grave E, Bakker DE, Vandenberghe R (1995): Influence of nonstoichiometry and the presence of maghemite on the Mössbauer spectrum of magnetite† vol 43

M. Hassan K, Dekan J (2013): Mössbauer study of Fe phases in terrestrial olivine basalts from southern Egypt vol 44

Marinho BA, Cristóvão RO, Loureiro JM, Boaventura RAR, Vilar VJP (2016) Solar photocatalytic reduction of Cr(VI) over Fe(III) in the presence of organic sacrificial agents. Appl Catal B Environ 192:208–219

Marinho BA, Cristóvão RO, Djellabi R, Loureiro JM, Boaventura RAR, Vilar VJP (2017a) Photocatalytic reduction of Cr(VI) over TiO_2-coated cellulose acetate monolithic structures using solar light. Appl Catal B Environ 203:18–30

Marinho BA et al (2017b) Intensification of heterogeneous TiO_2 photocatalysis using an innovative micro–meso-structured-reactor for Cr(VI) reduction under simulated solar light. Chem Eng J 318:76–88

Marinho BA, Cristóvão RO, Djellabi R, Caseiro A, Miranda SM, Loureiro JM, Boaventura RAR, Dias MM, Lopes JCB, Vilar VJP (2018) Strategies to reduce mass and photons transfer limitations in heterogeneous photocatalytic processes: hexavalent chromium reduction studies. J Environ Manag 217:555–564

McCammon C, Mitchell R, Chakhmouradian A (1999): Mossbauer spectra of priderite and synthetic iron-bearing hollandite vol 37

McCanta MC, Dyar MD (2017) Impact-related thermal effects on the redox state of Ca-pyroxene. Meteorit Planet Sci 52:320–332

McEnroe SA, Harrison RJ, Robinson P, Golla U, Jercinovic MJ (2001) Effect of fine-scale microstructures in titanohematite on the acquisition and stability of natural remanent magnetization in granulite facies metamorphic rocks, southwest Sweden: Implications for crustal magnetism. J Geophys Res Solid Earth 106:30523–30546

McEnroe S, Robinson P, Miyajima N, Fabian K, Dyar D, Sklute E (2016): Lamellar magnetism and exchange bias in billion-year-old titanohematite with nanoscale ilmenite exsolution lamellae: I. Mineral and magnetic characterization vol 206

Meichtry JM, Quici N, Mailhot G, Litter MI (2011) Heterogeneous photocatalytic degradation of citric acid over TiO2. I: mechanism of 3-oxoglutaric acid degradation. Appl Catal B Environ 102:454–463

Moon J, Bae S, Celik K, Yoon S, Kim K-H, Kim KS, PJM M (2014) Characterization of natural pozzolan-based geopolymeric binders. Cem Concr Compos 53:97–104

Morris RV, Golden DC, Bell JF, Lauer HV, Adams JB (1993) Pigmenting agents in martian soils: inferences from spectral, Mössbauer, and magnetic properties of nanophase and other iron oxides in Hawaiian palagonitic soil PN-9. Geochim Cosmochim Acta 57:4597–4609

Mytych P, Stasicka Z (2004) Photochemical reduction of chromium(VI) by phenol and its halogen derivatives. Appl Catal B Environ 52:167–172

Nozik AJ (1972) Mossbauer evidence for hole trapping by ferric acceptor states on rutile surfaces. J Phys C Solid State Phys 5:3147–3152

Omrane M, Kenai S, Kadri E-H, Aït-Mokhtar A (2017) Performance and durability of self compacting concrete using recycled concrete aggregates and natural pozzolan. J Clean Prod 165:415–430

Patel SKS, Kurian S, Gajbhiye NS (2012) Phase dependent room-temperature ferromagnetism of Fe-doped TiO_2 nanorods. AIP Adv 2:012107

Patil SB, Basavarajappa PS, Ganganagappa N, Jyothi MS, Raghu AV, Reddy KR (2019) Recent advances in non-metals-doped TiO_2 nanostructured photocatalysts for visible-light driven hydrogen production, CO_2 reduction and air purification. Int J Hydrog Energy 44:13022–13039

Pongwan P, Wetchakun K, Phanichphant S, Wetchakun N (2016) Enhancement of visible-light photocatalytic activity of Cu-doped TiO_2 nanoparticles. Res Chem Intermed 42:2815–2830

Qin R, Meng F, Khan MW, Yu B, Li H, Fan Z, Gong J (2019) Fabrication and enhanced photocatalytic property of TiO_2-ZnO composite photocatalysts. Mater Lett 240:84–87

Redhammer Günther J, Amthauer G, Roth G, Tippelt G, Lottermoser W (2006): Single-crystal X-ray diffraction and temperature dependent 57Fe Mössbauer spectroscopy on the hedenbergite-aegirine (Ca, Na)(Fe^{2+},Fe^{3+})Si_2O_6 solid solution vol 91

Rodríguez-Torres CE, Cabrera AF, Errico LA, Adán C, Requejo FG, Weissmann M, Stewart SJ (2008) Local structure and magnetic behaviour of Fe-doped TiO_2 anatase nanoparticles: experiments and calculations. J Phys Condens Matter 20:135210

Roonasi P, Mazinani M (2017) Synthesis and application of barium ferrite/activated carbon composite as an effective solar photocatalyst for discoloration of organic dye contaminants in wastewater. J Environ Chem Eng 5:3822–3827

Salim MMFF et al (2016) Photochemical UVC/H2O2 oxidation system as an effective method for the decolourisation of bio-treated textile wastewaters: towards onsite water reuse. RSC Adv 6:90631–90645

Sandin TR, Schroeer D, Spencer CD (1976) Mössbauer effect for 57Fe and 57Co in TiO_2 (rutile). Phys Rev B 13:4784–4789

Soares PA, Silva TFCV, Ramos Arcy A, Souza SMAGU, Boaventura RAR, Vilar VJP (2016) Assessment of AOPs as a polishing step in the decolourisation of bio-treated textile wastewater: technical and economic considerations. J Photochem Photobiol A Chem 317:26–38

Sorescu M, Xu T, Wise A, Díaz-Michelena M, McHenry M (2012): Studies on structural, magnetic and thermal properties of Fe_2TiO_4-Fe_3O_4 Pseudo-binary System vol 324

Stampel PP, Travis JC, Bielefeld MJ (1973): Mössbauer spectroscopic studies of iron-doped rutile physica status solidi (a) 15, 181–189

Tanaka H, Kono M (1987) Mössbauer spectra of titanomagnetite: a reappraisal. J Geomagn Geoelectr 39:463–475

Trejo-Valdez M, Hernández-Guzmán SR, Manriquez-Ramírez ME, Sobral H, Martínez-Gutiérrez H, Torres-Torres C (2019) Removal of aqueous chromium and environmental CO_2 by using photocatalytic TiO_2 doped with tungsten. J Hazard Mater 370:196–202

Valari M, Antoniadis A, Mantzavinos D, Poulios I (2015) Photocatalytic reduction of Cr(VI) over titania suspensions. Catal Today 252:190–194

Van Alboom A, De Grave E, Vandenberghe R (1991): Mossbauer study of the hematite phase formed during synthesis of ferri-diopsides vol 95

Wamba AGN et al (2017) Synthesis of grafted natural pozzolan with 3-aminopropyltriethoxysilane: preparation, characterization, and application for removal of Brilliant Green 1 and Reactive Black 5 from aqueous solutions. Environ Sci Pollut Res 24:21807–21820

Wang N, Zhu L, Deng K, She Y, Yu Y, Tang H (2010) Visible light photocatalytic reduction of Cr(VI) on TiO_2 in situ modified with small molecular weight organic acids. Appl Catal B Environ 95: 400–407

Wang Z, Zhang H, Cao H, Wang L, Wan Z, Hao Y, Wang X (2017) Facile preparation of ZnS/CdS core/shell nanotubes and their enhanced photocatalytic performance. Int J Hydrog Energy 42: 17394–17402

Wang D, Hou P, Yang P, Cheng X (2018a) BiOBr@SiO_2 flower-like nanospheres chemically-bonded on cement-based materials for photocatalysis. Appl Surf Sci 430:539–548

Wang L, Zhao J, Liu H, Huang J (2018b) Design, modification and application of semiconductor photocatalysts. J Taiwan Inst Chem Eng 93:590–602

Whipple ER (1974) Quantitative Mössbauer spectra and chemistry of iron. Massachusetts Institute of Technology

Xu W, Peacor Donald R, Dollase Wayne A, Van Der Voo R, Beaubouef R (1997): Transformation of titanomagnetite to titanomaghemite: a slow, two-step, oxidation-ordering process in MORB vol 82

Yan H, Wang X, Yao M, Yao X (2013) Band structure design of semiconductors for enhanced photocatalytic activity: the case of TiO_2. Pro Nat Sci-Mater 23:402–407

Yang J-K, Lee S-M (2006) Removal of Cr(VI) and humic acid by using TiO_2 photocatalysis. Chemosphere 63:1677–1684

Zeitler VA, Brown CA (1957) The infrared spectra of some Ti-O-Si, Ti-O-Ti and Si-O-Si compounds. J Phys Chem 61:1174–1177

Zhu S, Liu W, Fan C, Li Y (2005) Mössbauer study of nano-TiO_2 doped with Fe. Hyperfine Interactions 165:273–278

Affiliations

Aline M. Novack[1] · Glaydson S. dos Reis[2] · Fabíola V. Hackbarth[1] · Belisa A. Marinho[1] · Maja B. Đolić[3] · José A. B. Valle[1] · Carlos H. Sampaio[4] · Eder C. Lima[5] · Guillherme L. Dotto[6] · Antônio Augusto Ulson de Souza[1] · Vítor J. P. Vilar[7] · Selene M. A. Guelli Ulson de Souza[1]

[1] Laboratory of Mass Transfer, Federal University of Santa Catarina (UFSC), PO Box 476, Florianópolis, SC 88040-900, Brazil

[2] Graduate Program in Mine, Metallurgical, and Materials Engineering (PPGE3M), School of Engineering, Federal University of Rio Grande do Sul (UFRGS), Av. Bento Gonçalves 9500, Porto Alegre, RS, Brazil

[3] Faculty of Technology and Metallurgy, University of Belgrade, Karnegijeva 4, Belgrade 11000, Serbia

[4] Departament d'Enginyeria Minera, Industrial i TIC, Prof. Serra Húnter, Universitat Politècnica de Catalunya Barcelona Tech, Manresa, Barcelona, Spain

[5] Institute of Chemistry, Federal University of Rio Grande do Sul (UFRGS), Av. Bento Gonçalves 9500, Postal Box 15003, Porto Alegre, RS 91501-970, Brazil

[6] Environmental Processes Laboratory (LAPAM), Chemical Engineering Department, Federal University of Santa Maria (UFSM), Av. Roraima 1000, Santa Maria, RS 97105-900, Brazil

[7] Laboratory of Separation and Reaction Engineering - Laboratory of Catalysis and Materials (LSRE-LCM), Department of Chemical Engineering, Faculty of Engineering, University of Porto, Rua do Dr. Roberto Frias, 4200-465 Porto, Portugal